Analysis of Satellite Sea Surface Temperature Time Series in the Brazil-Malvinas Current Confluence Region: Dominance of the Annual and Semiannual Periods

Christine Provost

Laboratoire d'Océanographic Dynamique et de Climatologie, CNRS, Université Pierre et Marie Curie, Paris

Omar Garcia

Centro Nacional de Investigacion Científica y Tecnica, Bahia Blanca, Buenos Aires, Argentina

Véronique Garçon

Centre National de la Recherche Scientifique, UMR 39, Toulouse, France

We study the dominant periodic variations of sea surface temperature (SST) in the Brazil-Malvinas Confluence region from a satellite-derived data set compiled by Olson et al. (1988). This data set is composed of 202 sea surface temperature images with a 4 × 4 km resolution and extends over 3 years (from July 1984 to July 1987). Each image is a 5-day composite. The dominant signal, as already observed by Podesta et al. (1991), has a 1-year period. We first fit a single-frequency sinusoidal model of the annual cycle in order to estimate mean temperature, amplitude, and phase at 159 points uniformly distributed over the region. The residuals are generally small (less than 2°C). The largest departures from this cycle are located either in the Brazil-Malvinas frontal region or in the southeastern part of the region. Other periods in SST variations are identified by means of periodograms of the 159 residual time series in which the annual cycle has been substracted. The periodograms show that a semiannual frequency signal is present at almost every location. The ratio of the semiannual amplitude to the annual amplitude increases southward from 0% at 30°S to reach up to 45% at 50°S. In the south the semiannual signal creates an asymmetry, and the resulting (total) annual cycle has a cold period (winter) longer than the warm one (summer). In the frontal region the annual and semiannual signals have an important interannual variation. This semiannual frequency is associated with the semiannual wave present in the atmospheric forcing of the southern hemisphere. Differential heating over the mid-latitude oceans and the high-latitude ice-covered Antarctic Continent has been suggested as the cause of this semiannual wave (Van Loon, 1967).

1. Introduction

The region of the South Atlantic where the warm, salty Brazil Current encounters the cold, low-salinity Malvinas Current is called the Brazil-Malvinas Confluence region. It is located off the coasts Argentina and Uruguay between 30° and 50°S and out to 45°W. This region corresponds to the polar western boundary of the subtropical gyre of the South Atlantic [*Confluence Principal Investigators*, 1990]. It is a region of strong thermohaline contrast (the Brazil-Malvinas front) [*Legeckis and Gordon*, 1982; *Olson et al.*, 1988], intense mesoscale activity [*Cheney et al.*, 1983; *Gordon*, 1989; *Provost et al.*, 1989], and important thermodynamical role with water-mass formation through wintertime convection [*Gordon*, 1981].

So far, most studies of sea surface temperature (SST) satellite images in the confluence region have emphasized the complexity of the mesoscale surface structures. *Legeckis* [1978], using National Oceanic and Atmospheric Administration (NOAA) advanced very high resolution radiometer (AVHRR) imagery, found that the southward extension of the Brazil Current and eddy generation are highly variable in

time. Subsequently, *Legeckis and Gordon* [1982] observed eddy shedding in the confluence region and poleward pulsing of the Brazil Current between 38°S and 46°S with a time scale of approximately 2 months.

Olson et al. [1988] used a 3-year time series of NOAA AVHRR images to study the temporal variations of the location where the Brazil and Malvinas currents separate from the coast. For each of these currents, they built a time series of the intersection between the visually determined thermal front and the 1000-m isobath. They found that the mean separation latitude from the shelf break is 35.8°S ± 1.1° for the Brazil Current and 38°S ± 0.9° for the Malvinas Current. They estimated the ranges of the positions of the separation of these currents from the coast to be 930 and 850 km, respectively. These ranges are quite large in comparison to similar statistics for the Gulf Stream or the Kuroshio.

Here, we do not use SST variations as Lagrangian indicators of mesoscale motions; rather, we consider SST time evolutions as a component of the ocean-atmosphere system. Instead of following individual mesoscale features as done in the studies mentioned above, we investigate the variations of SST from an Eulerian point of view at 159 points regularly spaced in the region. This approach is similar to that of *Podesta et al.* [1991]. Our objective is to describe quantitatively the temporal variations of the SST in the Brazil-Malvinas Confluence region. We wish to identify the domi-

nant periods in SST variability, provide a clear image of SST variations in the region, and relate to ocean dynamics and atmospheric forcings.

SST is a key parameter of ocean-atmosphere interactions: it is the essential ocean parameter which controls the exchanges of heat between the ocean and the atmosphere. Surface heat flux and surface temperature are strongly related, and often, in the absence of reliable data on the surface heat fluxes, many ocean modelers have parameterized these in terms of observed sea surface temperature. SST is the only ocean parameter assimilated in atmospheric general circulation models (AGCM).

The contrasts in heat fluxes in the Brazil-Malvinas Confluence are strong: north of the Confluence the ocean looses heat to the atmosphere (warm Brazil Current); south of it the ocean gains heat to the atmosphere (cold Malvinas Current) [*Bunker*, 1988]. The estimates for these two local extrema in net annual heat fluxes are about -55 W/m^2 and $+50$ W/m^2 [*Bunker*, 1988]. Both the latent and sensible heat fluxes show local extrema on each side of the convergence and a distribution very reminiscent of the SST and surface flow patterns in the region [*Bunker*, 1988].

We use the same data set as *Olson et al.* [1988]. This data set is rapidly presented in section 2. It is a precious source of information as oceanic observations, and time series in particular, are scarce in the southern hemisphere. As already found by *Podesta et al.* (1991), a clear annual cycle appears to dominate SST variations. Using Bayesian inference, we first fit a single-frequency sinusoidal model of the annual cycle to obtain mean temperature, amplitude, and phase estimates of the 159 time series extracted at points regularly distributed in the region (section 3). Other periodic signals are identified through the calculation of the periodograms of the 159 time series (the annual frequency being subtracted) (section 4). Signals with a semiannual period are identified and described (section 5). Interannual variations are discussed with respect to their relation to frontal motions and eventual interannual general trends (section 6). A discussion follows in which we try to relate SST variations to variations of atmospheric forcings (section 7). We conclude this analysis in section 8.

2. DATA

2.1. Data Source and Data Accuracy

The data processing done at the Rosenstiel School of Marine and Atmospheric Science in Miami (RSMAS) to obtain this satellite-derived SST time series from the AVHRR is detailed by *Olson et al.* [1988] and *Podesta et al.* [1991]. The SST time series we analyzed spans 3 years from July 1984 to July 1987 and is made of 202 5-day composite images with an approximately 4 × 4 km resolution. The compositing of five successive daily images conserving for each pixel the warmest temperature observed during those 5 days reduces cloud coverage. It is generally considered that satellite-derived sea surface temperatures are now approaching 0.5°C in accuracy [*Bernstein and Chelton*, 1985; *Njoku*, 1985; *Njoku et al.*, 1985]. However, an additional problem here is the accuracy of the mosaics. In 5 days, the surface temperature can change locally by over 3°C, in the frontal region, for example. In the following, we will consider 3°C as the accuracy of the SST mosaic data. This value will prove to be too conservative.

2.2. Typical SST Images of the Region

Typical austral summer conditions are illustrated by the SST mosaic image from February 6 to 10, 1986 (Plate 1a). Along the coast, north of the estuary of the Rio de la Plata, the warm waters correspond to the Brazil Current. Surface temperatures reach values greater than 26°C. The temperatures in the estuary of the Rio de la Plata, are also high (22°–26°C). Surface temperature of the Malvinas Waters increases from below 7°C in the south to about 10°C to the north. The Malvinas Current, about 100 km wide, follows the 1000-m isobath. The Brazil and Malvinas currents meet at about 38°S, and their confluence creates large temperature gradients. A large warm elliptical eddy is centered at 54°W and 45°S.

Plate 1b corresponds to the mosaic image from July 11 to 16, 1986 (austral winter). The main structures of the surface temperature are similar to those of Plate 1a, although values are lower by more than 4°C.

2.3. Typical SST Time Series From the Region

In order to study temporal variations in the SST, 159 SST time series were extracted at the locations shown in Figure 1, i.e., every degree in latitude and longitude. Several of these SST time series are shown on Figure 2, they correspond to locations 3 (Figure 2a), 21 (Figure 2b), 42 (Figure 2c), 88 (Figure 2d), 84 (Figure 2e), and 159 (Figure 2f). In each the annual cycle is easily detected. The amplitude of the cycle, the values of the minimum and the maximum, the time of occurence of the minimum in the year, and the dispersion about the main cycle vary with location. Time series extracted at points on the continental shelf (locations 42 and 159, for example) exhibit very regular annual cycles with very different means (15.5°C and 9.5°C for locations 42 and 159, respectively) and amplitudes (11°C and 6.3°C for locations 42 and 159, respectively). The southern locations (84, 88, and 159) show long winters (cold water), and the warm period is more peaklike than sinusoidal. Although irregular variations in SST associated to frontal motions are evident at location 21, a seasonal cycle still dominates. In a first approach, we try to represent the annual cycle by a simple sinusoidal model with a single annual frequency.

3. SINUSOIDAL MODEL OF THE ANNUAL CYCLE

3.1. Method

Mean temperature, amplitude, and phase are obtained for each time series by fitting a sinusoidal curve. For each time series j, the observed satellite temperature $T_{ti,j}$ at time ti is written as

$$T_{ti,j} A_j = \tfrac{1}{2} \cos\left[(2\pi/365)(\text{ti} - j_j)\right] + b_j + \varepsilon_{ti,j} \quad (1)$$

where $T_{ti,j}$ is the temperature observed at point j at time ti, b_j is the mean temperature at point j, ti is the time (in days), φ_j is the phase (in days), and $\varepsilon_{ti,j}$ is the residual at each data point.

For each time series, we minimize the quantity

$$R_j = \Sigma_{ti}(\varepsilon_{ti,j})^2 \quad (2)$$

This is a nonlinear least square problem.

We solve it using Bayesian inference. Bayesian inference
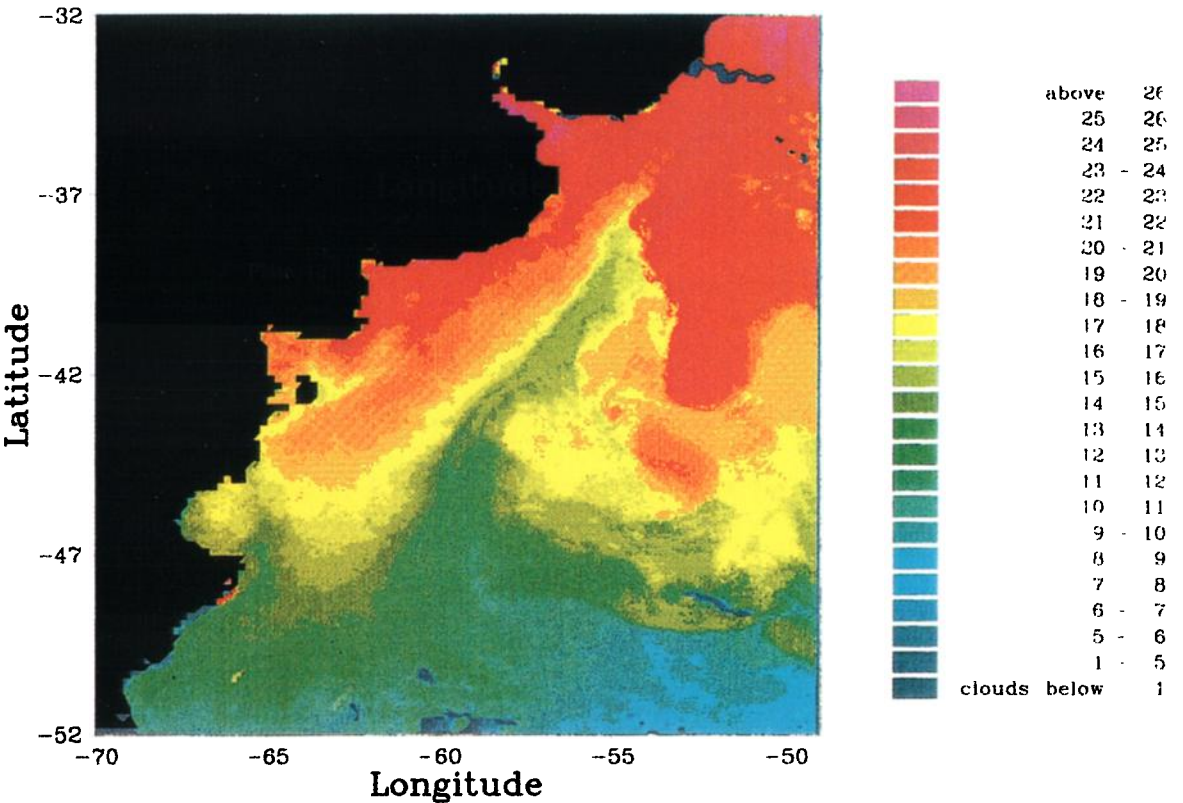
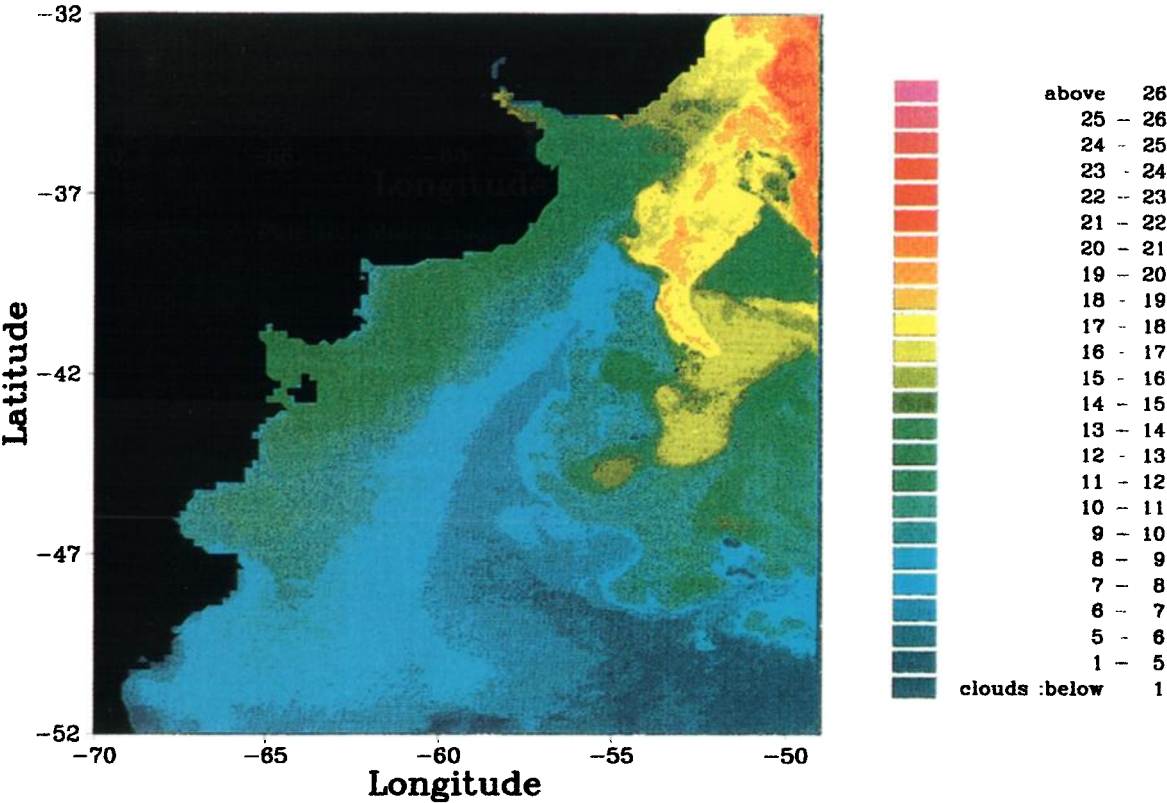Plate 1a.   Mosaic image from February 6 to 10, 1986 (austral summer).

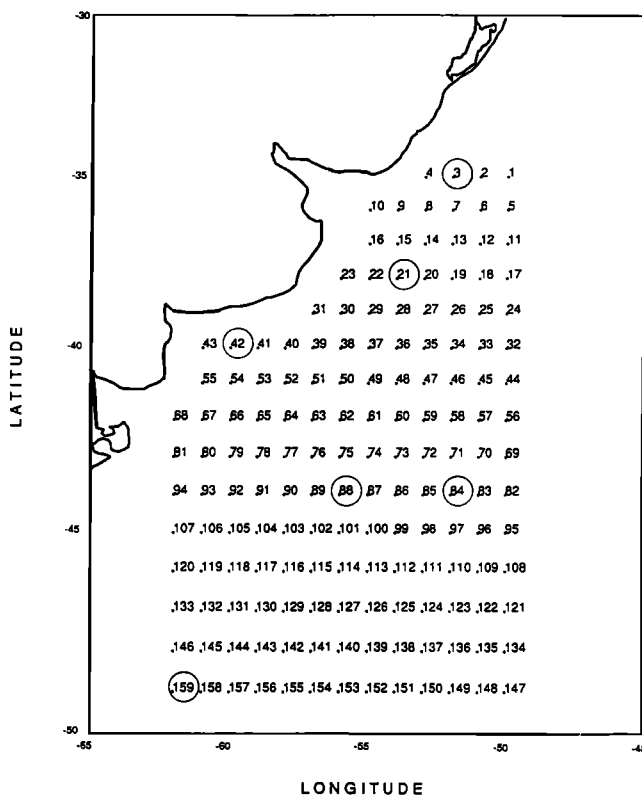Plate 1b.   Mosaic image from July 11 to 16, 1986 (austral winter).

Fig. 1. Locations of the 159 time series of SST that were extracted (every degree of latitude and longitude). The six time series corresponding to the circles are shown on Figure 2.

has been used in regression problems in geophysics [e.g., *Backus*, 1988] or in image analysis [e.g., *Geman and Geman*; 1987]. The Bayesian estimate is defined as the most probable value of the parameters given two ingredients: (1) a functional relationship between the data and the parameters and (2) an a priori probability distribution law for the parameters.

Here the relationship between the data T_j and the parameters (A_j, b_j, φ_j) is given by (1). We explicitly assume that the mean value of each parameter (α, β, ϕ) has a uniform distribution and that measurement errors are independent and have a normal distribution with variance s.

The procedure consists then, of three nested loops exploring wide ranges of possible values (α, β, ϕ) for A_j, b_j, and φ_j with small iterative increments. For each triplet (α, β, ϕ) we compute the residuals R (α, β, ϕ) and, according to Bayes' theorem the joint posterior probability density is

$$P(\alpha, \beta, \phi) = 1/\sigma^n \exp \{[R^2(\alpha, \beta, \phi)/2\sigma^2]\} \quad (3)$$

where n is the number of observations in the time series j and σ is the standard deviation of the SST measurement errors estimated here as 1.5°C (3°C/2).

We then obtain the following estimations for A, b, and φ and their respective variances:

$$A_{j\,est} = \Sigma_{(\alpha,\beta,\phi)}\alpha * P(\alpha, \beta, \phi)/\Sigma_{(\alpha,\beta,\phi)}P(\alpha, \beta, \phi) \quad (4a)$$

$$\text{Var } A_{j\,est} = \Sigma_{(\alpha,\beta,\phi)}(\alpha - A_{j\,est})^2$$

$$* P(\alpha, \beta, \phi)/\Sigma_{(\alpha,\beta,\phi)}P(\alpha, \beta, \phi) \quad (4b)$$

$$\varphi_{j\,est} = \Sigma_{(\alpha,\beta,\phi)}\phi * P(\alpha, \beta, \phi)/\Sigma_{(\alpha,\beta,\phi)}P(\alpha, \beta, \phi) \quad (4c)$$

$$\text{Var } \varphi_{j\,est} = \Sigma_{(\alpha,\beta,\phi)}(\phi - \varphi_{j\,est})^2$$

$$* P(\alpha, \beta, \phi)/\Sigma_{(\alpha,\beta,\phi)}P(\alpha, \beta, \phi) \quad (4d)$$

$$b_{j\,est} = \Sigma_{(\alpha,\beta,\phi)}\beta * P(\alpha, \beta, \phi)/\Sigma_{(\alpha,\beta,\phi)}P(\alpha, \beta, \phi) \quad (4e)$$

$$\text{Var } b_{j\,est} = \Sigma_{(\alpha,\beta,\phi)}(\beta - b_{j\,est})^2$$

$$* P(\alpha, \beta, \phi)/\Sigma_{(\alpha,\beta,\phi)}P(\alpha, \beta, \phi) \quad (4f)$$

For each parameter, the variance corresponds to a density probability of 68%. The standard deviation, associated to a 95% density probability, is equal to twice the variance.

Covariances are calculated in the same manner. For example, the covariance between the amplitude and the mean is defined as:

$$\text{Cov } (A_j, b_j) = \Sigma_{(\alpha,\beta,\phi)}(\alpha - A_{j\,est})(\beta - b_{j\,est})$$

$$* P(\alpha, \beta, \phi)/\Sigma_{(\alpha,\beta,\phi)}P(\alpha, \beta, \phi) \quad (4g)$$

We initiate the search with relatively large increments between successive trial values (0.5°C for α, 0.5°C for β, and 5 days for ϕ). We repeat the procedure three times, with increments smaller and smaller each time. The final increments are 0.01°C for α (amplitude of the sinusoidal cycle) and β (mean temperature) and 1 day for ϕ (phase). The 0.01°C increment chosen for α and β is much smaller than the accuracy of SST images and the 1-day increment for the phase is small enough since we are using 5-day composite images.

3.2. Results

The maximum length for any time series is 219 points. This corresponds to one 5-day composite image during 3 years. The number of data available is always less than 190 due to cloud cover (Figure 3). The 170 data point isoline corresponds to 25% of the data missing. The structures in Figure 3 are mainly meridional, with a number of points which is maximum on the shelf (over 180) and which decreases toward the ocean interior (down to 130 in the southeast). The drop out of data to the east is affected by the location of the ground station (Villa Ortuzar, in Buenos Aires). In the far east region, there are fewer passes going into the compositing leading to less cloud removal and poorer coverage.

The residuals (Figure 4) from the sinusoidal Bayesian fit are always less than 2°C except in two regions. In the area corresponding to the Malvinas-Brazil Front (a meridional band from 35°S to 45°S and centered around longitude 54°.5W) residuals can reach up to 3°C. Departures from the sinusoidal curve are due to frontal motions and shedding of warm rings by the Brazil Current. These departures are exemplified in the time series shown in Figure 5b which corresponds to location 21 (38°S and 54°W). The other region with residuals larger than 2°C is located east of 53°W and south of 47°S where residuals are probably associated with motions of the subantarctic front [*Peterson and Whitworth*, 1989].

Residuals are less than 1.4°C on the shelf, where satellite-derived SST's follow closely a sinusoidal cycle. At location 159 (Figure 5f) the global residual is less than 1°C, and the largest departures from the single-frequency sinusoidal cycle probably correspond to eddies passing by.
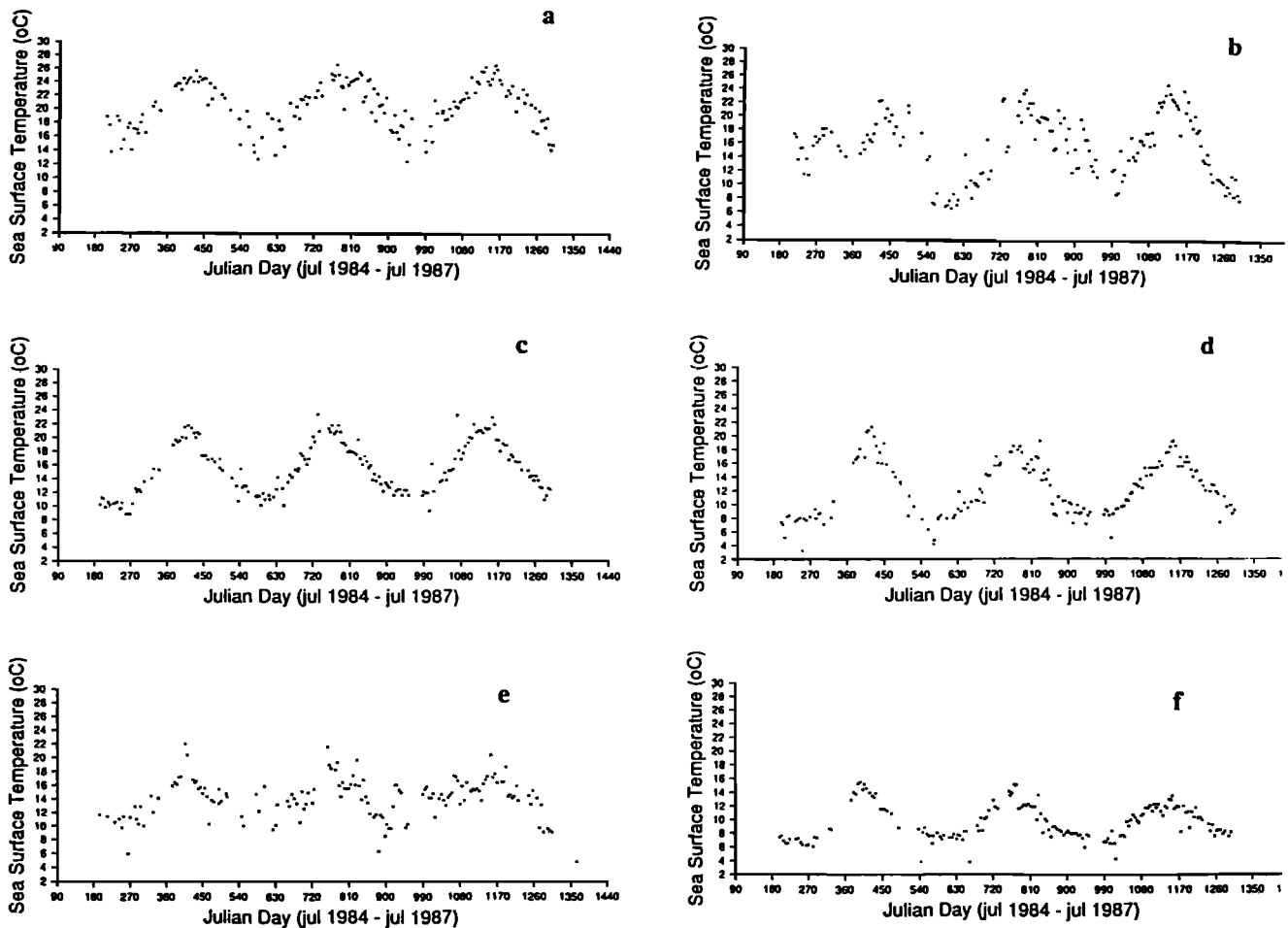
Fig. 2.   SST time series corresponding to locations (a) 3, (b) 21, (c) 42, (d) 88, (e) 84, and (f) 159.

The resulting distribution of the mean temperature (Figure 6a) shows the basic large-scale temperature structures of the region: a cold Malvinas current (with average temperatures less than 12°C) following the continental slope and the warm Brazil Current (temperature above 18°C) to the north. The standard deviation of the mean temperature estimator (Figure 6b) is always less than 0.3°C and increases from the coast offshore (as the number of data points decreases).

The amplitude of the sinusoidal model is maximum on the shelf (Figure 7a). Ranges of variation (i.e., twice the amplitude) higher than 11°C are found on the shelf at the latitude of the mouth of the Rio de la Plata. The general tendency is a decrease in amplitude from the coast offshore and from the north to the south. The amplitude is larger where the contrast is larger between the air and water temperatures. A noticeable maximum of 10°C is found in the core of the Malvinas Current at the latitude of 43°S. The cold Malvinas water advected into a region where summer is relatively warm gets warmed up easily at the surface. There, a very shallow (about 10–30 m deep) and very steep (ΔT about 10°C) seasonal thermocline develops in summer in agreement with observations made during the Confluence 3 experiment (February 1990) [Provost et al., 1991]. The range of variations in SST is small both in the north (away from the coast influence) in the Brazil Current (about 7°C), and in the south (6°C). The warm Brazil Current remains in a relatively warm region throughout the year, whereas cold waters in the

south remain in a cold environment. The standard deviation of the amplitude estimator is always less than 0.7°C with the lower values found in the south (0.54°C) (Figure 7b).

The phase is difficult to interpret (Figure 8a). The phase refered to January 1 is everywhere between 25 days (at the level of the front, at 40°S and 54°W) and 60 days (in the Brazil Current at 37°S and 53°W). In reality, most locations exhibit phase values between 40 and 50 days, which means that the highest summer temperature is reached 40 to 50 days after the beginning of the year, i.e., around mid-February. The strong local minimum which appears associated with the front is risky to interpret because of the poor fit there (large residuals). Apart from that controversial minimum, one can observe a general tendency for lower values on the continental shelf and in the South. This would mean that the highest summer temperature is reached 10 days earlier on the shelf and in the south than in the Brazil Current.

The standard deviation of the phase estimator (Figure 8b) has a mean of 10 days which is good since we only have a data point every 5 days. The small value of the variance of the phase estimator near the coast is logical with the better fit obtained there. The small variance at points where residuals are large, like in the frontal region, indicates that although signals with other periods are important there, the annual cycle is unambiguous and clearly defined. Although a sinusoidal cycle with a single annual frequency seems to explain accurately most of the temporal variations of the satellite
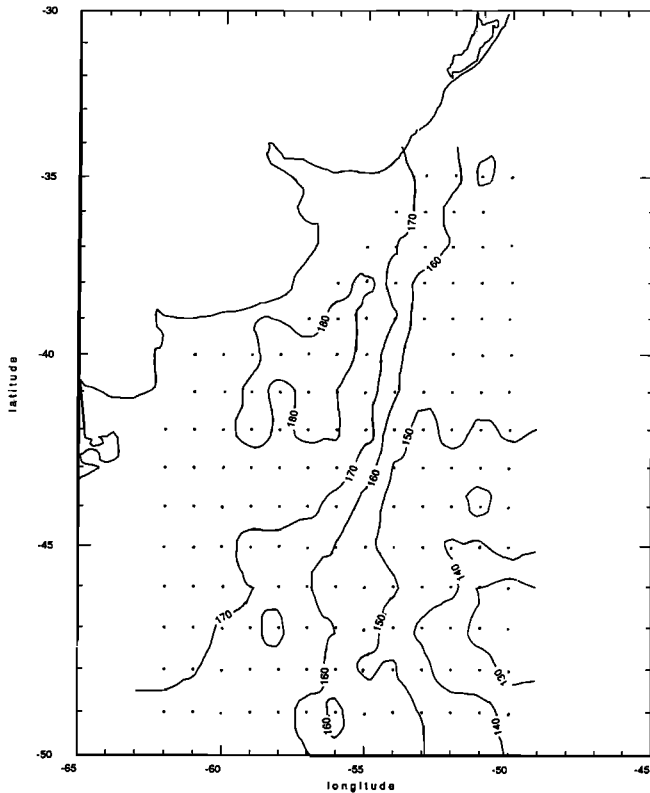
Fig. 3.   Number of data available at each location.

The normalized periodogram (spectral power as a function of angular frequency $\omega = 2\pi f$) is then defined by

$$P_N(\omega) = 1/2\sigma^2 \frac{[\Sigma_j(T_j - T)^2 \cos \omega(t_j - \tau)]}{\Sigma_j \cos^2\omega(t_j - \tau)}$$

$$+ \frac{[\Sigma_j(T_j - T)^2 \sin \omega(t_j - \tau)]^2}{\Sigma_j \sin^2\omega(t_j - \tau)} \quad (6)$$

where τ is defined by the relation

$$\tan (2\omega\tau) = \Sigma_j \sin 2\omega t_j/\Sigma_j \cos 2\omega t_j \quad (7)$$

The constant τ is similar to a time offset that makes $P_N(\omega)$ completely independent of shifting all the t_i by any constant. *Lomb* [1976] has shown that this particuliar choice of offset makes equation (6) identical to the equation that one would obtain if one would estimate the harmonic content of a data set, at a given frequency ω, by linear least squares fitting to the model:

$$T(t) = A \cos \omega t + B \sin \omega t \quad (8)$$

This fact gives some insight into why the method can give results superior to FFT methods: it weights the data on a per-data-point basis instead of a per-time-interval basis, when uneven sampling can render the latter seriously in error.

A very nice property of the Scargle normalized periodogram is that it allows to quantitatively assess the signifi-

derived SSTs (with the exception of the frontal area and the southeast), one can easily distinguish other periodic signals in the residual time series presented in Figure 5.

4. OTHER PERIODIC SIGNALS

The standard way to study the periodic signals in a time series is to compute its power spectra. However, mainly because of cloud cover, the SST data are unevenly spaced in time. Therefore standard methods based on fast Fourier transform (FFT) cannot be used. An obvious way to get around the problem is to do some kind of temporal interpolation to obtain evenly spaced data and then use FFT methods. This method performs poorly, especially whenever there is a long gap in the data. A completely different method of spectral analysis for unevenly sampled data was developed by *Lomb* [1976] and *Scargle* [1982].

4.1. Method

This novel type of periodogram (Fourier spectrum) analysis is quite powerful for finding and testing the significance of weak periodic signals in otherwise random, unevenly sampled data. *Horne and Baliunas* [1986] have elaborated on the method and discussed its implementation. The Lomb-Scargle periodogram evaluates data, and sines and cosines, only at times t_i that are actually measured. Briefly, given a set of data values, T_i $i = 1, \cdots N$ at respective observational times t_i, the Lomb-Scargle periodogram is constructed as follows.

First, the mean and variance of the data are computed:

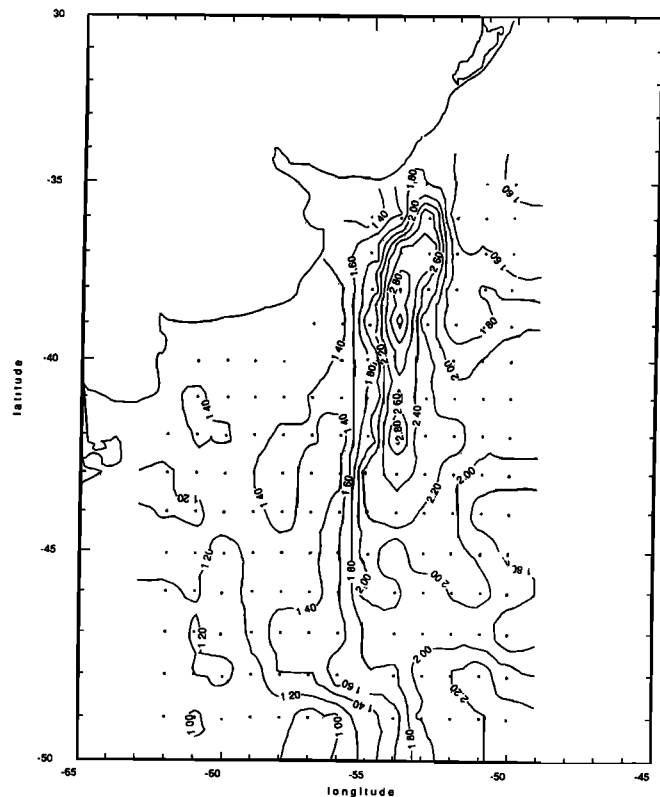$$T = 1/N\Sigma T_i, \qquad \sigma^2 = 1/(N - 1)\Sigma(T_i - T)^2 \quad (5)$$

Fig. 4.   Residuals from the single frequency sinusoidal Bayesian inference (in degrees Celsius). They are smaller than 2°C except in the region of the Malvinas-Brazil Front (a meridional band from 35°S to 45°S and centered on longitude 54°.5W with values up to 3°C) and in the southeast. Residuals are less than 1.4°C on the shelf.
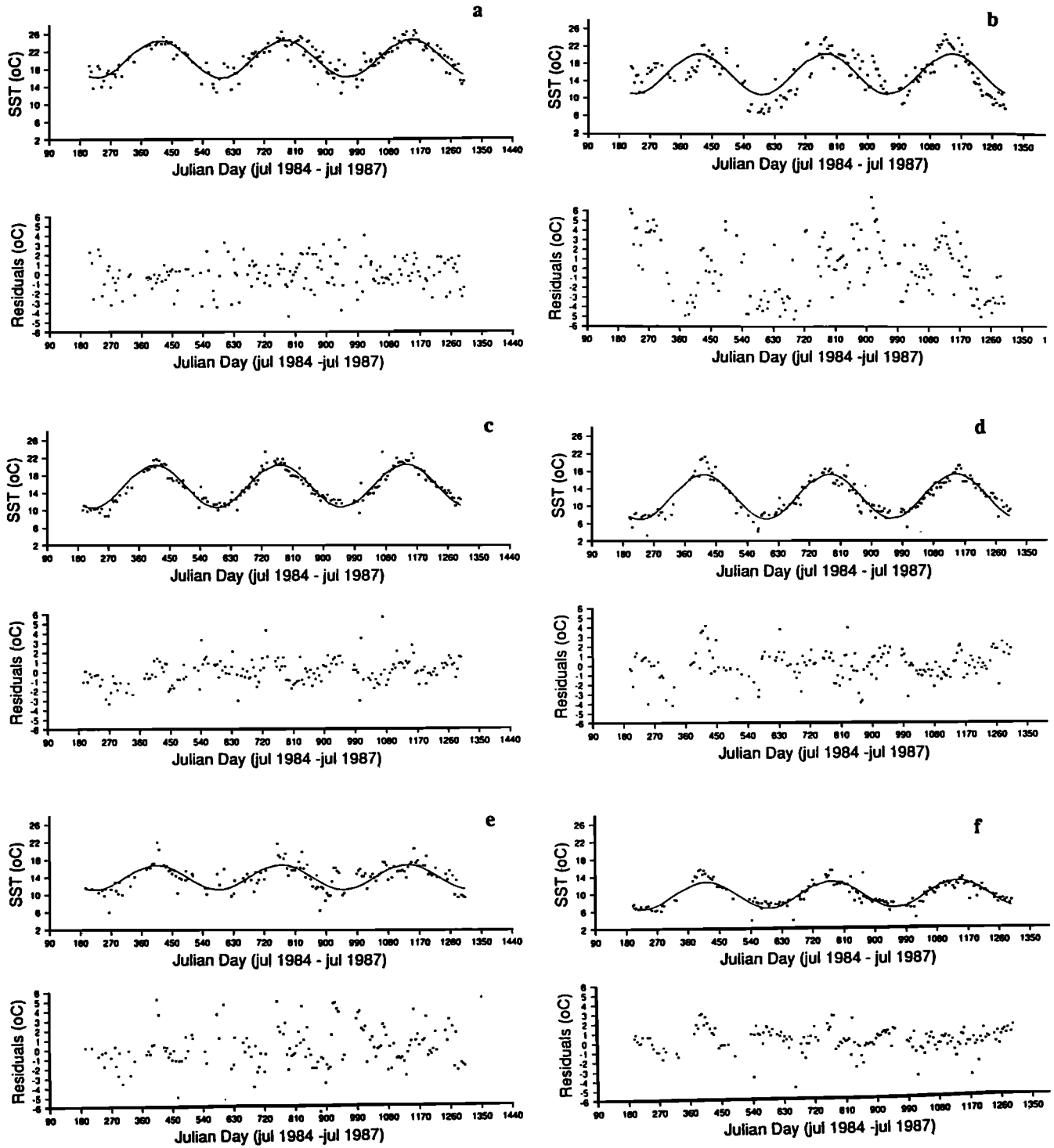
Fig. 5.   Time series at locations (a) 3, (b) 21, (c) 42, (d) 88, (e) 84, and (f) 159 with the corresponding sinusoidal fit and the residuals.

cance of a peak in the spectrum $P_{N(\omega)}$. The word "normalized" refers to the factor σ^2 in the denominator of equation (6). Scargle [1982] shows that with this normalization, the probablity that $P_{N(\omega)}$ be between some positive z and $z + dz$ is exp $(-z)dz$. Therefore, if we scan M independent frequencies, the probability that none gives values larger than z is $(1 - \exp (-z))^M$. So

$$P(>z) = 1 - [1 - \exp (-z)]^M \qquad (9)$$

is the significance level of any peak in $P_N(\omega)$ that we do see. In fact, equation (9) can be series expanded to give

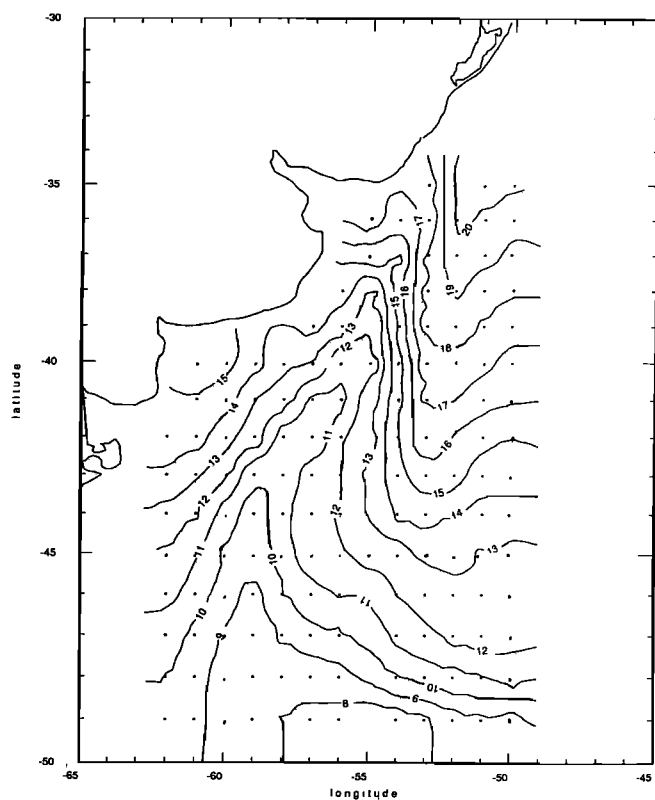$$P(>z) = M \exp (-z) \qquad (10)$$

Fig. 6a. Estimate of the mean temperature from the Bayesian inference (in degrees Celsius).
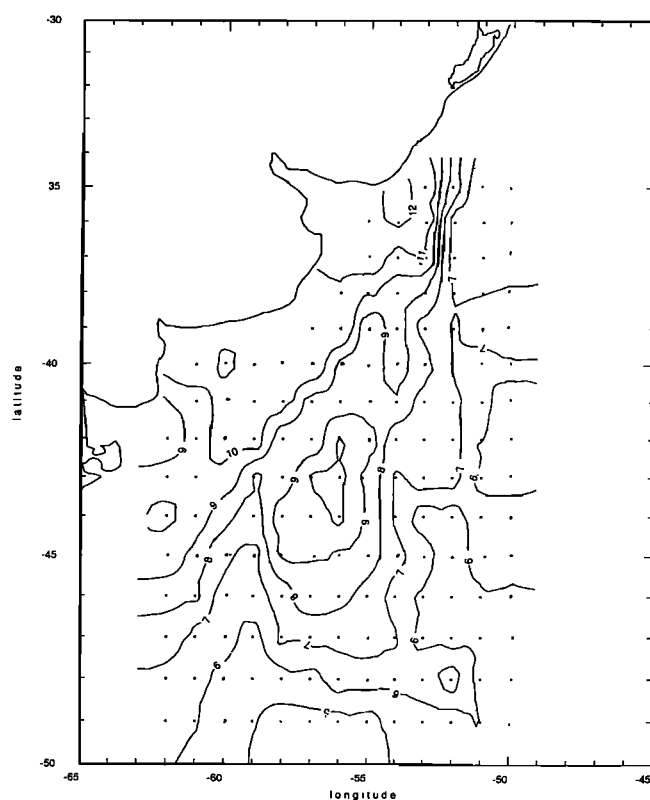

Fig. 7a. Amplitude of the annual sinusoidal signal from the Bayesian inference (in degrees Celsius).
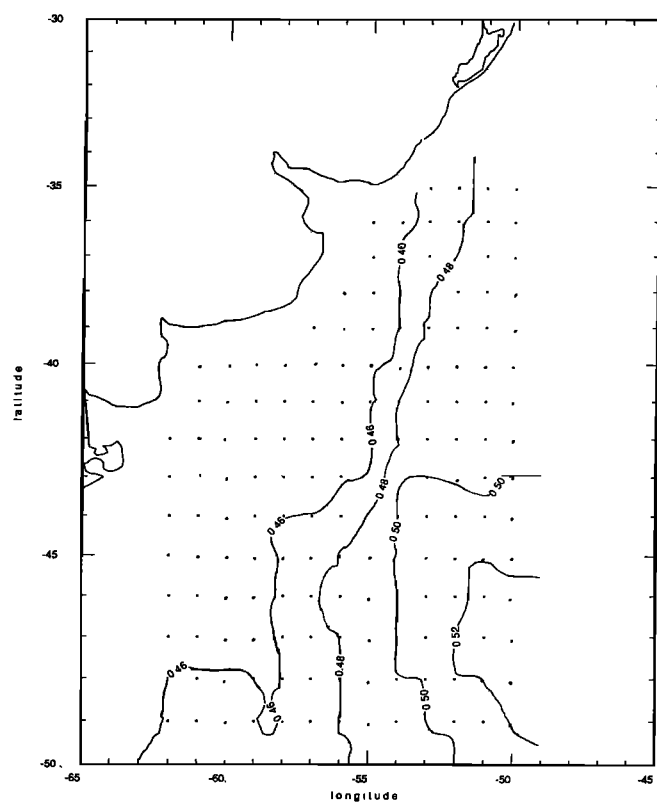

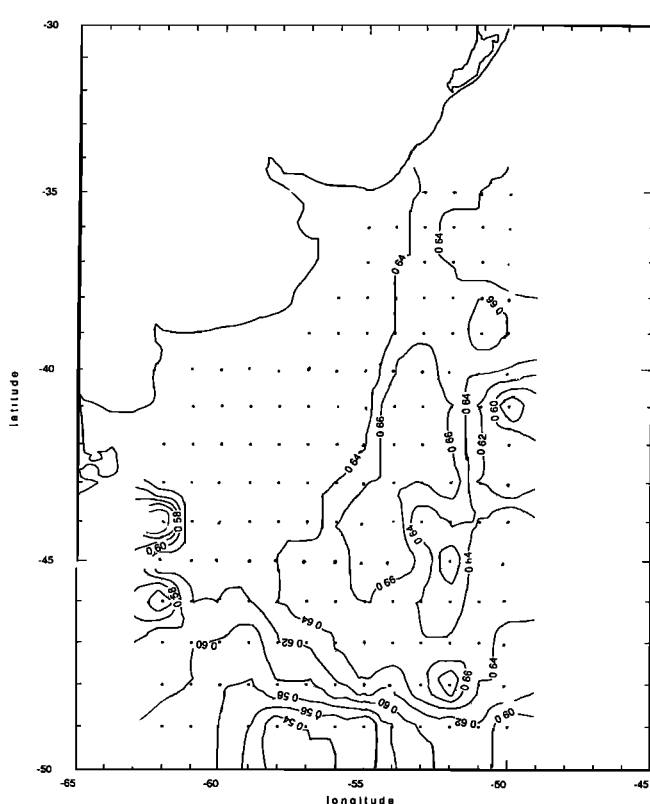Fig. 6b. Standard deviation of the mean temperature estimator (in degrees Celsius).

Fig. 7b. Standard deviation of the amplitude estimator (in degrees Celsius).

and to the first order, the significance level varies linearly with M. We see therefore that the estimate of M, the number of independent frequencies, does not need to be very accurate. *Horne and Baliunas* [1986] have shown that M is very nearly equal to N and depends on the distribution of the unevenly spaced data. They have shown that

$$N < M < M_{max} \qquad (11)$$

where M_{max} is given by the empirical formula

$$M_{max} = -6.362 + 1.193N + 0.00098N^2$$

M being difficult to compute, we have calculated the significance levels associated with the probabilities 50%, 90%, 99% and 99.9% with $M = N$ and with $M = M_{max}$. We therefore obtain for each probability (50, 90, 99, and 99.9%) the maximum and the minimum significance levels. In fact, the difference between the significance levels associated to M or M_{max} is very small, always less than 10%. We only represented the more optimistic value, i.e., the one associated with N.

If the periodogram shows a peak at the pulsation ω_0, *Horne and Balunias* [1986] give an expression of the incertitude $\delta\omega$ on this pulsation:

$$\delta\omega = (3\pi\sigma_N)/(2N^{1/2} * T * A) \qquad (12)$$

where σ_N is the variance of the data after removing the periodic signal observed, A is the range of the corresponding signal and T is the total temporal range covered by the time series [*Horne and Balunias*, 1986]. The expression for this variance is given by *Ferraz-Mello* [1981]:
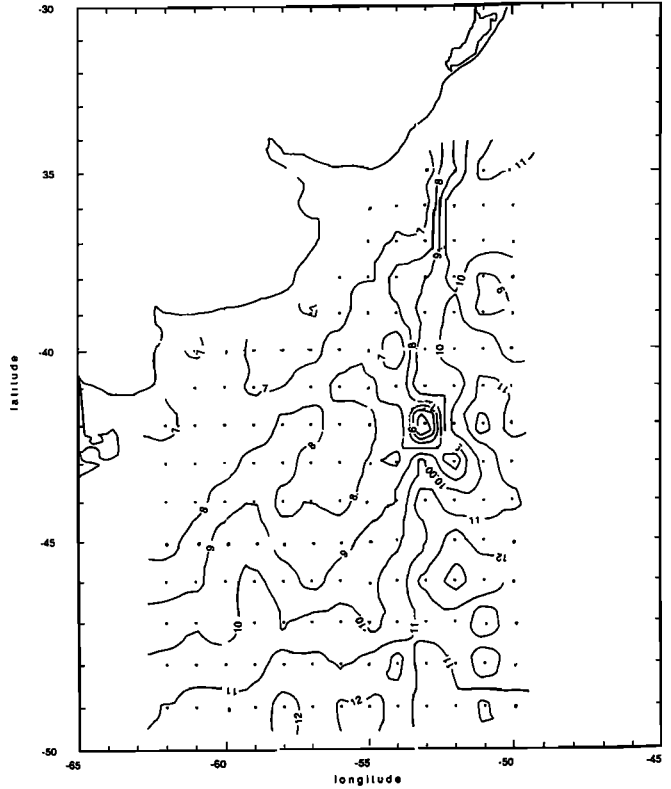
$$\sigma_N^2 = \sigma^2 - I(\omega_0)/N \qquad (13)$$

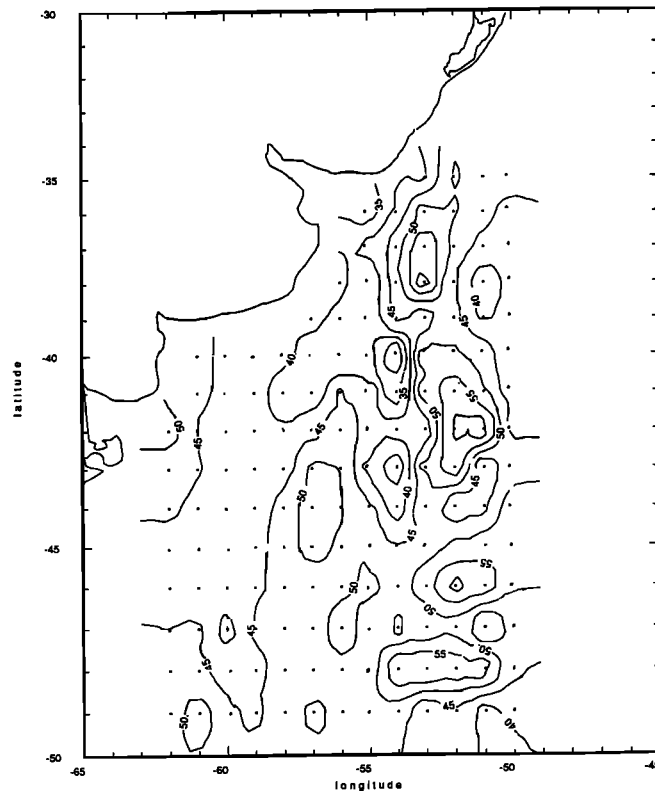Fig. 8b. Standard deviation of the phase estimator (in days).

with

$$I(\omega_0) = c_1^2 + c_2^2$$

and

$$c_1 \# (2N^{1/2}) \Sigma_j T_j \cos (\omega_0 t_j)$$

$$c_2 \# (2N^{1/2}) \Sigma_j T_j \sin (\omega_0 t_j)$$

σ^2 being the total variance of the data.

The periodogram has two inconveniences: it is rather costly in computing time and is subject to spectral leakage, i.e., the dominant peak does not appear only at the pulsation ω_0 but also at other pulsations. Therefore, one has to be cautious and interpret only the highest peak. When looking at other signals, it is better to substract the first periodic signal from the original data and recompute the periodogram.

4.2. Annual Frequency

The periodograms obtained from time series 3, 21, 42, 88, 84, and 159 are shown in Figure 9 as a function of pulsation (cycles per day). Four significance levels are represented: they correspond to probabilities of 50%, 90%, 99%, and 99.9% and are calculated with a number of independent frequencies equal to the number of data points in the series. The annual peak is much higher than the 99.9% significance level. This result is general: in each of the 159 periodograms, the annual signal dominates with an amplitude much larger than the significance level corresponding to a probability of 99.9%. For each time series, the amplitude of the peak corresponding to the annual period is nicely equal to the

Fig. 8a. Phase of the single frequency annual cycle from the Bayesian inference (in days).
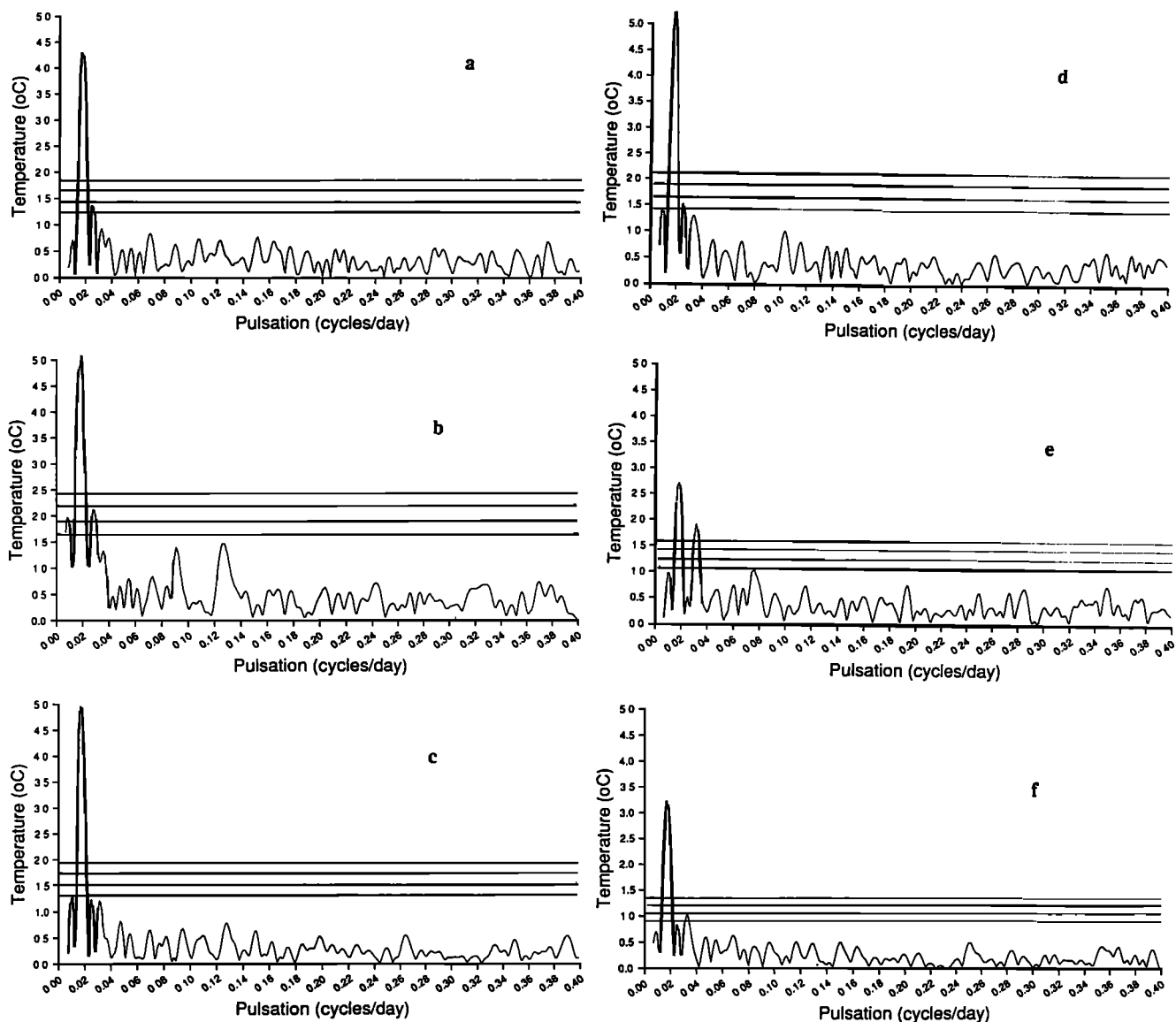
Fig. 9. Periodograms of the full time series at locations (a) 3, (b) 21, (c) 42, (d) 88, (e) 84, (f) 159. Four levels of significance are represented: 99.9%, 99%, 90%, and 50%.

respective amplitude found with the Bayesian inference at the corresponding location (Figure 7a).

Often other frequencies have a larger amplitude than the significance level corresponding to a probability of 90%. However, these must be interpreted carefully. To avoid problems in interpretation due to the spectrum leakage, we calculate the periodograms of the residual time series after having removed the annual cycle from the data.

4.3. Other Frequencies

The periodograms of the 159 time series of the residuals have been calculated. They can be classified in five main groups according to whether they do not present any significative peak (group 1), whether their largest peak is exactly at a period of 6 months (group 2), whether their largest peak is obtained at periods longer than a year (group 3), whether their largest peak is at periods shorter than a year but longer than 6 months (group 4), whether their largest peak is at periods shorter than 6 months (group 5). The spatial distri-

bution of these different groups is shown in Figure 10a, whereas the level of significance of the largest peak is shown in Figure 10b.

The first group (periodograms without any significant peak) contains only five time series. All five are located in the north (Figure 10a). At these points the annual cycle looks like a sinusoid with all seasons of equal duration, and the residuals obtained in section 3 are less than 1.80°C. For example, all the peaks in the periodogram of the residuals at location 3 are below the 50% significance level (Figure 11a). This means that the residuals obtained in section 3 are approximately randomly distributed (Figure 5a).

In the second type of periodograms, the largest peak is obtained at the semiannual frequency (183 ± 6 days). This behavior is the most frequent and the group contains 81 time series out of the 159, i.e., 51%. This concerns most of the locations west of 54W and most of the locations south of 45S (Figure 10a). Most of the periodograms belonging to that group have their largest peak above the 99.9% significance
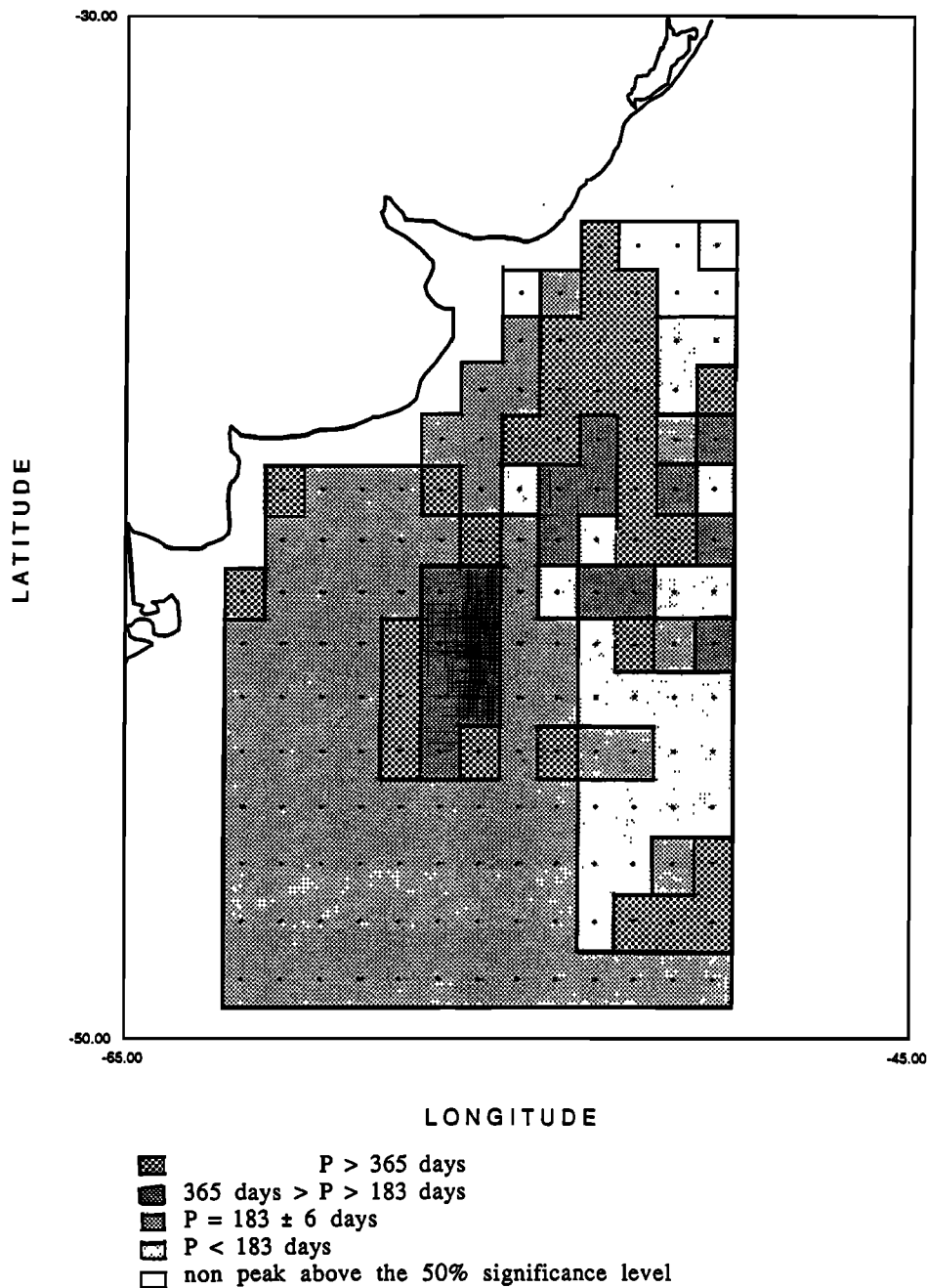
Fig. 10a.   Spatial distribution of the different behavior for the periodograms of the residual time series.

level (Figure 10b). Time series 42 belongs in that group: the largest peak is above the 99.9% significance level (Figure 11c), and it has an amplitude of 0.78°C and is at pulsation 0.034. This corresponds to a period of 185 ± 6 days, i.e., a semiannual period. All other signals are below the 50% confidence limit. Time series number 159 (Figure 11f) presents the same characteristic features (one single dominant period at 185 ± 6 days and an amplitude of 0.9°C, above the 99.9% level).

The periodograms of the third type have their highest peak at a period larger than the annual period. This might be an indication of interannual variability. This is a rather small group (28 time series over 159 i.e. 17%) ubiquitous of the frontal region (Figure 10a). The highest peak is not always very significant (only 50% of them are above 99.9%). (Figure

10b) and is accompanied with other peaks at or close to the semiannual frequency. Time series number 21 (Figure 11b) is an example. Three pulsations have an amplitude larger than 99.9% significance level. The highest peak with an amplitude of 2.25°C is at a period between 700 and 800 days, i.e., 2 years. When looking back at the original time series (Figure 2b) or at the residual time serie (Figure 5b), one readily sees that the first part of the time series contains a strong isolated event (probably an isolated frontal excursion or a large eddy passing by). The second peak (2.20°C) at 217 days and the third peak (2.03°C at 305 days) are probably modulations of the semiannual frequency.

The fourth type corresponds to periodograms with the largest peak at a period between a year and 6 months.

S > 99.9% significance level

99.9 % > S > 99%

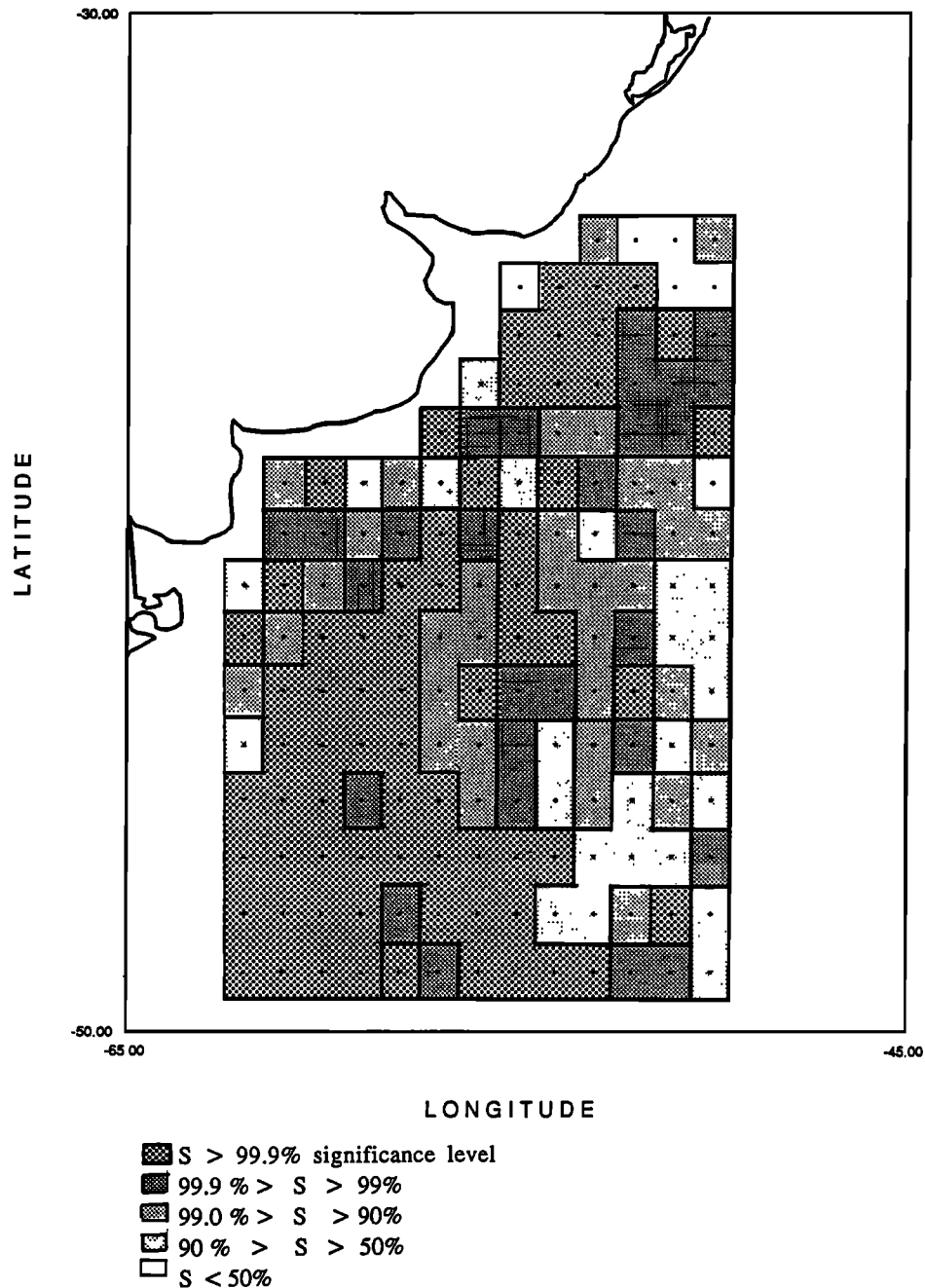99.0 % > S > 90%

90 % > S > 50%

S < 50%

Fig. 10b.   Spatial distribution of the level of significance of the largest peak of the periodograms of the residual time series.

Usually, these periodograms also exhibit a significant peak at the semiannual period. This behavior concerns only 11% (17) of the 159 time series. They are located in the center of the region (Figure 10a). The level significance of the largest peak is not always above 90% (Figure 10b). Time series 88 (Figure 11d) has its largest peak at 286 days (0.82°C) and a second one at 180 days (0.78°C) both being between the 99% and 99.9% significance levels.

The fifth group (24 time series, i.e., 15%) contains periodograms which have their largest peak at periods smaller than 6 months. They all correspond to locations east of 55W (Figure 10a) and the dominant peak is not always above the

99% (Figure 10b). Usually in these periodograms, the semiannual peak is significant too. The dominant period varies between 40 and 100 days. Most of the elements of this group have their peak at about 70–80 days. Time series 84 is an example of this behavior (Figure 11e). The largest peak (1.35°C) is obtained at a pulsation of 0.078, i.e., 80 ± 2 days. A weaker peak (1.28°C) is present at the semiannual frequency. Both peaks are above the 99.9% significance level.

Although it may be dominated or modulated by other frequencies, the semiannual frequency is clearly significant in more than 80% of the time series. Section 5 is an attempt to describe and interpret this semiannual signal.
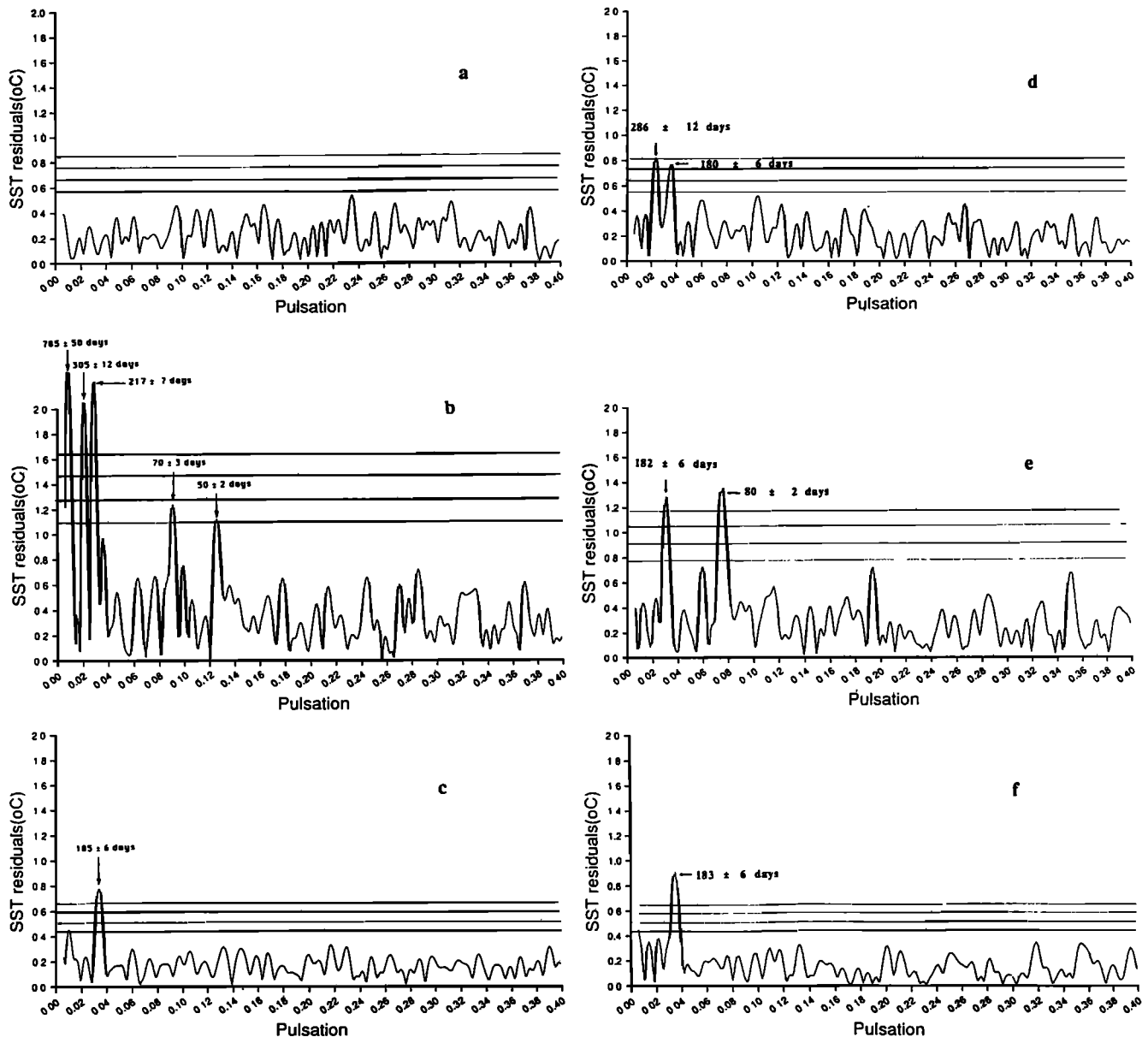
Fig. 11.   Periodograms of the residual time series at locations (a) 3, (b) 21, (c) 42, (d) 88, (e) 84, (f) 159. The same four levels of significance are represented 99.9%, 99%, 90%, and 50%.

5. SEMIANNUAL PERIOD

An annual signal made up of two frequencies (annual and semiannual) is fitted to the data using Bayesian inference with five unknowns (amplitudes and phases for the semiannual and annual and mean). The global misfit (Figure 12a) is, of course, smaller than in the single frequency fit (Figure 4), roughly by about 0.2°C. The improvement is noticeable in the western and southern part of the region. West of 56°W the global misfit is less than 1.4°C. The structures in Figure 12a are similar to those of Figure 4, i.e., with a large misfit in the frontal region. Estimates of the mean temperature and of the amplitude and phase of the annual frequency do not change significantly.

The range of variation of the semiannual component (twice the amplitude) (Figure 12b) varies between 0.4°C and 2.8°C. The standard deviation associated with this estimate

is always between 0.5°C and 0.7°C. The amplitude of the semiannual component is minimum in the north (Brazil Current) and in most coastal locations (less than 1°C range, i.e., less than 0.3°C amplitude). These locations comprise all time series of group 1 (no peak above 50% significance) and part of the time series of group 2 (dominant period shorter than the semiannual period) in the Brazil Current. Two other regions, an elongated one in the center along 58°W and another one to the east, are local minima (range less than 1°C). The elongated region is clearly associated with the Malvinas Current. The amplitude of the semiannual signal has a local maximum in the frontal region: clearly frontal motions have a 6-month period component.

The ratio of the amplitude associated with the semiannual frequency to the amplitude associated with the annual one is easier to interpret (Figure 12c). It has a clear west-east

north-south structure: in the north and in the west the amplitude of the semiannual component is less than 15% of the amplitude of the annual component. In the south it reaches 40%. A minimum (less than 10%) associated with the return flow breaks this north-south and west-east general increase tendency. The 15% isoline seems to correspond to the northern limit of some influence from southern origin.

The phase associated with the semiannual component has a large standard deviation between 20 days in the southeast and more than 60 days in the north. In the north and along the coast the semiannual cycle does not exist so we get 100% error on the phase. In the south the standard deviation of the phase estimate is between 15 and 30 days.

Phase estimates can be interpreted after looking at each of the time series and seeing how the semiannual component recombines with the annual component in order to make up for the full annual signal responsible for the small misfit in Figure 12a. The time series examples shown earlier are represented in Figure 13 with their components: annual frequency (dotted curve), semiannual component (dashed curve), and full annual cycle (solid curve). Over the whole region, the semiannual component creates an asymmetry in the total annual cycle and combines with the annual component to make winters longer than summers. This asymmetry between summer and winter is, of course, stronger in the south than in the north of the domain.

6. DISCUSSION

In this section we discuss some implications of our results and related results of previous studies to the dynamics of the confluence region.
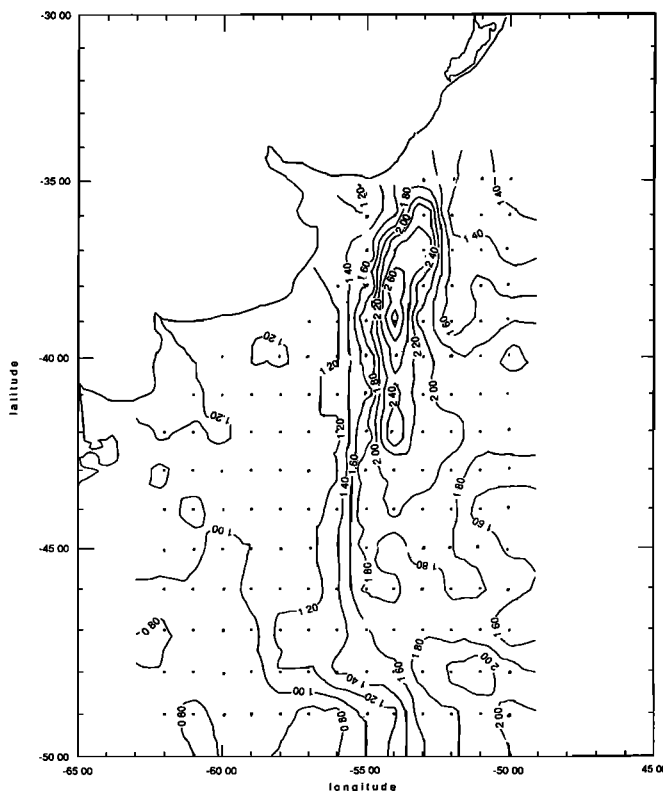

Fig. 12a. Residuals after fitting with an annual cycle made up of an annual and a semiannual frequency (in degrees Celsius).
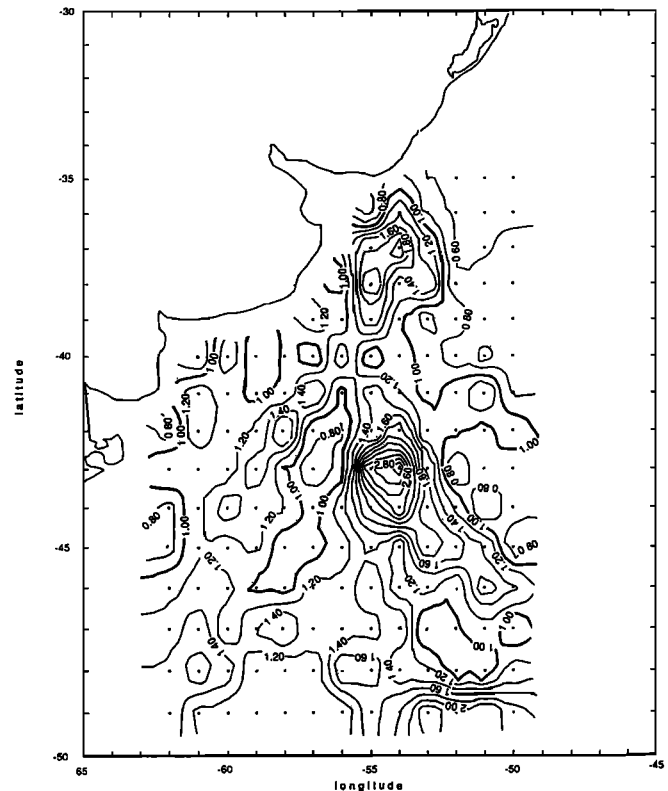

Fig. 12b. Estimate of the range (2 × amplitude) of the semiannual component (in degrees Celsius).

6.1. Atmosphere

We first recall a few characteristics of the atmospheric circulation in the southern hemisphere and then in the confluence region. In addition, to the well-documented annual wave (first harmonic) in the atmosphere, the existence of a strong second harmonic (semiannual) wave in the southern hemisphere is well established. The importance of the half-year wave in the southern hemisphere was discovered in climate analyses of sea level pressure based on sparse observations [Van Loon, 1966]. This half-year wave has been observed in various fields in the atmosphere: in the temperature [Van Loon, 1967], in the pressure [Van Loon, 1967, 1972a; Van Loon et al., 1972; Hsu and Wallace, 1976], in the wind [Van Loon, 1967, 1972b; Large and Van Loon, 1989], and in the precipitation [Van Loon, 1972c]. The annual wave in sea level pressure (SLP) (as well as the semiannual wave in zonal wind or wind stress) is largest in the latitudes near 30°S over and near continents where it also explains most of the variance [Van Loon, 1972a, b, c, 1984; Van Loon and Rogers, 1984b]. It is secondary to the semiannual over most of middle and high southern latitudes. The semiannual wave is a marked feature of the southern hemisphere atmospheric circulation and dominates the shape of the annual curve of SLP, geostrophic wind, and temperature gradient in the troposphere poleward of the subtropical ridge (30°S).

A complete explanation of this wave has not yet been given. Van Loon [1967] related it to the difference in heating in oceanic middle and continental high latitudes. These differences appear in the troposphere as a semiannual wave in the meridional temperature gradient which has a maxima
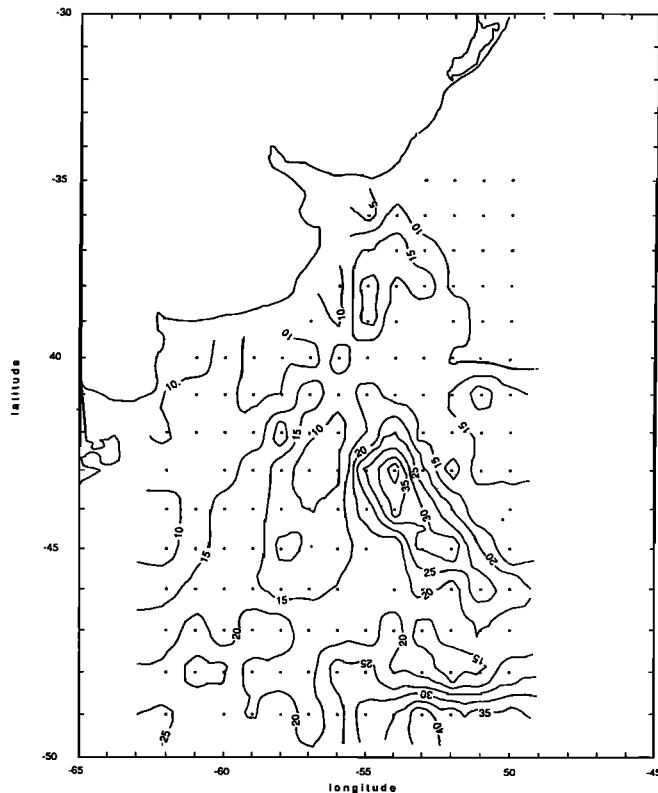
Fig. 12c. Ratio of the amplitude of the semiannual cycle to the amplitude of the annual cycle (in percent).

in the transitional seasons at mid-latitudes: the meridional gradient of air temperature between the mid-latitudes: the meridional gradient of air temperature between the mid-latitudes and the polar region becomes large in spring and autumn because of their differences in the annual march of the temperature. Since changes of the meridional temperature gradient are changes of baroclinicity, the semiannual variation of the temperature gradient is associated with a semiannual variation of cyclonic activity and thus of the mean SLP.

The semiannual wave in SLP at Port Stanley (Falkland Islands 52°S, 58°W, just 2° south of the region studied here) represents only 30% of the total variance (probably due to the presence of the South American continent), whereas it explains over 70% in other middle latitude open-ocean locations of the southern hemisphere [Van Loon and Rogers, 1984a]. Here we find that the ratio of half-year wave to the yearly wave in SST increases southward from 0% at 30°S to 30–40% at 50°S.

Interannual variations in the yearly wave and in the half-yearly cycle of SLP and zonal geostrophic wind and wind stress have been described by Van Loon and Rogers [1984a, b]. The yearly and half-yearly waves in pressure and zonal wind have all large interannual variations, especially at mid-latitudes.

As we could not find any time series of meteorological fields in the Confluence region, the only data we could have tried to correlate SST with were outputs from atmospheric general circulation models (AGCM). However, AGCMs fail to reproduce this half-yearly wave faithfully when they are run freely over extended period. Comparisons of SLP with European Center for Medium range Weather Forecast (EC-

MWF) T21 AGCM are reported by Von Storch and Xu [1987]. The model adequately reproduces the amplitude and phase of the annual phase, but the semiannual wave is too small in amplitude and has unrealistic phase. Other comparisons with other AGCM including those of the Geophysical Fluid Dynamics Laboratory, the National Center for Atmospheric Research, and the Canadian Climate Centre have the same shortcomings [Xu et al., 1988].

It is possible that the semiannual wave signals in the atmosphere represent a coupled mode of the ocean-atmosphere system. As such they would not be expected to appear in AGCM simulation where SST is prescribed.

This absence of reliable semiannual wave in the southern hemisphere circulations produced by present AGCMs is a serious problem ocean general circulation models (OGCM) have to face. If the semiannual signals are not correct in the atmospheric forcings, then the ocean will not be forced properly.

6.2. Oceanic Measurements

The annual and semiannual signals have been suggested by few authors. The FGGE drifting buoy array has revealed highly significant large-scale, low-frequency variability in the zonal drift of the buoys [Large and Van Loon, 1989]. The variability (strong semiannual and significant annual signals) appears to be related to the wind, and Large and Van Loon argue that the buoy drift may prove to be representative of the surface currents at large scale and low frequency.

From year-long time series obtained from three inverted echosounders (IES), Garzoli and Garraffo [1989] were able to calculate the dynamic height of the surface relative to 800 m and estimate the location of the Brazil-Malvinas front. In spite of the short duration of the time series, their results suggest a 6-month oscillation superimposed on the main displacement of the front that has a 12-month period. This main displacement is east-west, and they associated it to variability in the latitude of maximum northward penetration of the Malvinas Current. They also detected a 1–2 month period signal that they associated to a north-south variation of the latitude of the return of the Brazil Current.

The shorter-period SST signals we observe are essentially located to the east of the domain and have amplitudes smaller than those of the semiannual variations. Usually, these shorter-period signals are seen on the residual time series as local events of short duration. The periodicity is generally between 60 and 80 days. This should be cautiously compared with the 1–2 month period for frontal motions found by Garzoli and Garraffo [1988] in their IES data analysis. Here, the 2–3 month period corresponds to a small amplitude change in SST and not to frontal signature. The Brazil-Malvinas subsurface front seen by the inverted echo sounders does not correspond to the maximum gradient in SST and does not have similar variations. In summer, surface warming creates a thin layer that hides the position of the main front from the surface [Provost et al., 1990]. So far, there does not exist any long-term ocean in situ time series to confront our analysis with and which could help discuss possible interannual variations.

7. CONCLUSION

The lack of long time series of observations both in the atmosphere and in the ocean in the southern hemisphere
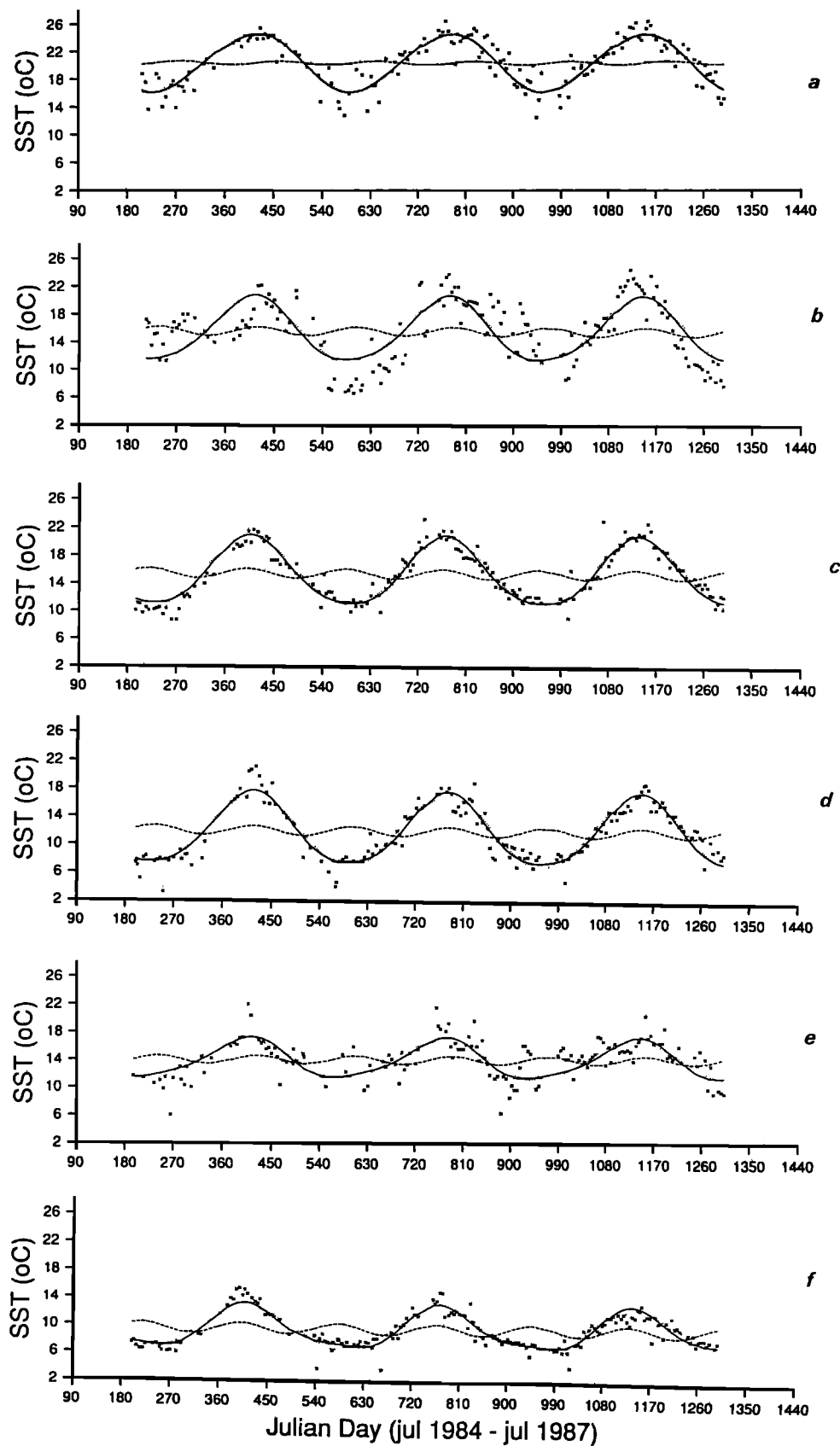
Fig. 13. Time series (a) 3, (b) 21, (c) 42, (d) 88, (e) 84, and (f) 159 with their two component the semiannual (dashed curve) the annual (dotted curve), and the combination of the two (solid curve). The residuals of each time series are also shown.

makes the *Olson et al.* [1988] satellite-derived SST time series over the Brazil-Malvinas Confluence region a particularly valuable data set. The time series we analyzed here was 3 years long and was made of 5-day composite images with a 4 × 4 km resolution [*Olson et al.* 1988].

It was a surprise for us to observe that in a region of intense mesoscale activity like the Malvinas-Brazil Current Confluence, SST variations are dominated by low-frequency variations. SST can be accurately described by an annual cycle made up of an annual frequency and a semiannual frequency. An SST field of the confluence region can be constructed for any day of the year from the two-frequency model with an accuracy of 1.4°C at any location except in the frontal region where the uncertainty on the estimates is of 3°C.

The annual component dominates everywhere. *Matano* [1991] has studied the seasonal variations of the Brazil-Malvinas Confluence with a wind forced barotropic numerical model of the South Atlantic and showed an increase of the transport by the Brazil Current in summer. This seasonal increase, i.e., southward motion of warm water, certainly adds up to the regular seasonal to create the large amplitudes in the northern part of the region.

The ratio of the amplitude of the semiannual component to that of the annual component increases southward from 0 to 45%. The semiannual frequency acts to make winter longer than summer: in the south, where the semiannual component is important, time series have an asymmetric shape with summers appearing as short peaks. The semiannual component, from its geographical distribution, seems to be associated with the annual and semiannual waves that dominate the atmospheric circulation in the southern hemisphere. The ratio of the half-yearly to the yearly amplitudes in SLP is small at 30°S and estimated to be 30% at 52°S in the confluence region [*Van Loon and Rogers*, 1984a]. Because of the lack of data and the poor performances of atmospheric general circulation models in the southern hemisphere, we were not able to correlate variations in SST with atmospheric fields.

Beyond these dominant semiannual and annual frequencies, we have been able to detect in the SST time series other periods: an interannual period and shorter periods of a few months. All the locations where interannual variations dominate semiannual ones are in the frontal region. We do believe, as already suggested by *Olson et al.* [1988], that the Malvinas and Brazil SST fronts have cyclical excursions along the coast at the semiannual and the annual periods, although with considerable interannual variations. In those 3 years of data, we could not detect other interannual variability than the one in the frontal region. However, we do believe that as the time series gets longer, small interannual variations will be detectable.

A strong limitation of our analysis is that the only other source of temperature time series available in the region (i.e., AGCMs) is unable to reproduce the half-yearly wave correctly in the southern hemisphere. This failure of AGCM will be a serious problem for ocean circulation models which will not be forced properly.

REFERENCES

Backus, G., Bayesian inference in geomagnetism, *Geophys. J.*, *92*, 125–142, 1988.

Bernstein, R. L., and D. B. Chelton, Large-scale sea surface temperature variability from satellite and shipboard measurements, *J. Geophys. Res.*, *90*, 11,619–11,630, 1985.

Bunker, A. F., Surface energy fluxes of the South Atlantic Ocean, *Mon. Weather Rev.*, *116*, 809–823, 1988.

Cheney, R. E., J. G. Marsh, and B. D. Beckley, Global mesoscale variability from collinear tracks of Seasat altimetry data, *J. Geophys. Res.*, *88*, 4343–4351, 1983.

Confluence Principal Investigators, Confluence 1988–1990: An intensive study of the southwestern Atlantic; Eos Trans. *AGU*, *71*(41), 1131–1134, 1990.

Ferraz-Mello, S., Estimation of periods from unequally spaced observations, *Astron. J.*, *86*, 456–463, 1981.

Garzoli, S., and Z. Garraffo, Transports, frontal motions and eddies at the Brazil-Malvinas Currents confluence, *Deep Sea Res.*, *36*, 681–703, 1989.

Geman, S., and D. Geman, Stochastic relaxation, Gibbs distributions, and the Bayesian restoration of images, *IEEE Trans. Pattern Anal. Mach. Intel.*, *PAMI-6*, 712–741, 1987.

Gordon, A. L., South Atlantic thermocline ventilation, *Deep Sea Res.*, *28A*, 1239–1264, 1981.

Gordon, A. L., Brazil-Malvinas confluence 1984, *Deep Sea Res.*, *36*, 359–384, 1989.

Horne, J. H., and S. L. Baliunas, A prescription for analysis of unevenly sampled time series, *Astrophys. J.*, *263*, 835–853, 1986.

Hsu, C. P. F., and J. M. Wallace, The global distribution of the annual and semi-annual cycles in sea level pressure, *Mon. Weather Rev.*, *104*, 1597–1601, 1976.

Large, W. G., and H. Van Loon, Large scale, low frequency variability of the 1979 FGGE surface buoy drifts and winds over the southern hemisphere, *J. Phys. Oceanogr.*, *19*, 216–232, 1989.

Legeckis, R., A survey of worldwide sea surface temperature fronts detected by environmental satellites, *J. Geophys. Res.*, *83*, 4501–4522, 1978.

Legeckis, R., and A. L. Gordon, Satellite observations of the Brazil and Falkland currents—1975 to 1976 and 1978, *Deep Sea Res.*, *29*, 375–401, 1982.

Lomb, N. R., Least squares frequency analysis of unequally spaced data, *Astrophys. Space Sci.*, *39*, 447–462, 1976.

Matano, R. P., A numerical study of the circulation in the South Atlantic Ocean, Ph.D. thesis, Princeton Univ., Princeton, N. J., 1991.

Njoku, E. G., Satellite-derived sea surface temperature: Workshop comparisons, *Bull. Am. Meteorol. Soc.*, *66*, 274–281, 1985.

Njoku, E. G., T. P. Barnett, R. M. Laurs, and A. C. Vastano, Advances in satellite sea surface temperature measurement and oceanographic applications, *J. Geophys. Res.*, *90*, 11,573–11,586, 1985.

Olson, D. B., G. P. Podesta, R. H. Evans, and O. B. Brown, Temporal variations in the separation of Brazil and Malvinas currents, *Deep Sea Res.*, *35*, 1971–1990, 1988.

Peterson, R. G., and T. Whitworth, The subantarctic and polar fronts in relation to deepwater masses through the southwestern Atlantic, *J. Geophys. Res.*, *94*, 10,817–10,845, 1989.

Podesta, G. P., O. B. Brown, and R. H. Evans, The annual cycle of satellite derived sea surface temperature in the southwestern Atlantic Ocean, *J. Clim.*, *4*, 457–467, 1991.

Provost, C., L. Mémery, and B. Torres Lista, Confluence 3: Données CTD-02, *Rapp. Interne LODYC91/02*, 188 pp., Lab. d'Océanogr. Dyn. et de Climatol., Paris, 1990.

Scargle, J. D., Studies in astronomical time series analysis, II, Statistical aspects of spectral analysis of unevenly spaced data, *Astrophys. J.*, *263*, 835–853, 1982.

Van Loon, On the annual temperature range over the southern oceans, *Geogr. Rev.*, *56*, 497–515, 1966.

Van Loon, H., The half-yearly oscillations in middle and high southern latitudes and the coreless winter, *J. Atmos. Sci.*, *24*, 472–486, 1967.

Van Loon, H., Pressure in the southern hemisphere, in *Meteorology of the Southern Hemisphere, Meteorol. Monogr.*, vol. 35, edited by C. W. Newton, pp. 59–86, American Meteorological Society, Boston, Mass., 1972a.

Van Loon, H., Wind in the southern hemisphere, in *Meteorology of the Southern Hemisphere, Meteorol. Mongr.*, vol. 35, edited by C. W. Newton, pp. 59–86, American Meteorological Society, Boston, Mass., 1972b.

Van Loon, H., Cloudiness and precipitation in the southern hemisphere, in *Meteorology of the Southern Hemisphere, Meteorol. Monogr.*, vol. 35, edited by C. W. Newton, pp. 59–86, American Meteorological Society, Boston, Mass., 1972c.

Van Loon, H., Interannual variations in the half yearly cycle of pressure gradients and zonal wind at sea level on the southern hemisphere, *Tellus, 36A*, 76–86, 1984.

Van Loon, H., and J. C. Rogers, Interannual variations in the half yearly cycle of pressure gradients and zonal wind at sea level on the southern hemisphere, *Tellus, 36A*, 76–86, 1984a.

Van Loon, H., and J. C. Rogers, The yearly wave in pressure and zonal geostrophic wind at sea level on the southern hemisphere and its interannual variability, *Tellus, 36A*, 348–354, 1984b.

Van Loon, H., K. Labitzke, and R. J. Jenne, Half yearly wave in the stratosphere, *J. Geophys. Res., 77*, 3846–3855, 1972.

Von Storch, H. V., and J. Xu, Southern hemisphere: Comparison with observed sea level pressure: Climate simulations with the ECMWF T21 model in Hamburg, Large scale modelling, *Rep. 1*, Meteorol. Inst. der Univ., Hamburg, 1987.

Xu, J. S., H. Von Storch, and H. Van Loon, The performance of four spectral GCMs in the southern hemisphere: The January and July climatology and the semi-annual wave, *Rep. 24*, Max-Planck-Ins. für Meteorol., Hamburg, 1988.

O. Garcia, CONICET, CRIBABB, 12 de octubre 1865, 8000 Bahia Blanca, Buenos Aires, Argentina.

V. Garçon CNRS, UMR39, 18 avenue Edouard Belin, 31055 Toulouse, France.

C. Provost, CNRS, LODYC, Universite P. et M. Curie, Tour 14 2E, 4 place Jussieu, 75235 Paris Cedex 05, France.